

## *Spitzer* IMAGING AND SPECTRAL MAPPING OF THE OXYGEN-RICH SUPERNOVA REMNANT G292.0+1.8

PARVIZ GHAVAMIAN<sup>1</sup>, KNOX S. LONG<sup>2</sup>, WILLIAM P. BLAIR<sup>3</sup>, SANGWOOK PARK<sup>4</sup>, ROBERT FESEN<sup>5</sup>, B. M. GAENSLER<sup>6</sup>, JOHN P. HUGHES<sup>7</sup>, JEONGHEE RHO<sup>8</sup>, AND P. FRANK WINKLER<sup>9</sup>

(Accepted February 23, 2012)  
*Draft version March 23, 2021*

### ABSTRACT

We present mid-infrared continuum and emission line images of the Galactic oxygen-rich supernova remnant (SNR) G292.0+1.8, acquired using the MIPS and IRS instruments on the *Spitzer Space Telescope*. The MIPS 24  $\mu\text{m}$  and 70  $\mu\text{m}$  images of G292.0+1.8 are dominated by continuum emission from a network of filaments encircling the SNR. The morphology of the SNR, as seen in the mid-infrared, resembles that seen in X-rays with the *Chandra* X-ray Observatory. Most of the mid-infrared emission in the MIPS images is produced by circumstellar dust heated in the non-radiative shocks around G292.0+1.8, confirming the results of earlier mid-IR observations with AKARI. In addition to emission from hot dust, we have also mapped atomic line emission between 14  $\mu\text{m}$  and 36  $\mu\text{m}$  using IRS spectral maps. The line emission is primarily associated with the bright oxygen-rich optical knots, but is also detected from fast-moving knots of ejecta. We confirm our earlier detection of 15-25  $\mu\text{m}$  emission characteristic of magnesium silicate dust in spectra of the radiatively shocked ejecta. We do not detect silicon line emission from any of the radiatively shocked ejecta in the southeast of the SNR, possibly because that the reverse shock has not yet penetrated most of the Si-rich ejecta in that region. This may indicate that G292.0+1.8 is less evolved in the southeast than the rest of the SNR, and may be further evidence in favor of an asymmetric SN explosion as proposed in recent X-ray studies of G292.0+1.8.

*Subject headings:* ISM: individual (G292.0+1.8), ISM: kinematics and dynamics, shock waves, plasmas, ISM: supernova remnants

### 1. INTRODUCTION

Oxygen-rich supernova remnants (SNRs) are objects whose optical spectra are dominated by oxygen forbidden line emission (i.e., [O I], [O II] and [O III]). This emission arises in radiative shocks in the oxygen-rich ejecta expelled from the core-collapse supernova (SN) explosion. G292.0+1.8, which is the result of an unrecorded SN that took place about 3000 years ago (Ghavamian, Hughes & Williams 2005; Winkler & Long 2006), is one of only seven such O-rich SNRs known today. In [O III]  $\lambda 5007$  optical images G292.0+1.8 is dominated by a distinct, crescent-shaped structure approximately  $1'$  in size (hereafter the ‘Spur’) located on the eastern side of the SNR (Goss et al. 1979). A collection of localized clumps (fast-moving knots, or FMKs, similar to those seen in Cas A) have also been found in the interior of G292.0+1.8 (Ghavamian, Hughes & Williams 2005; Winkler & Long

2006). This contrasts with the appearance of the SNR at X-ray (Clark, Tuohy & Becker 1980; Park et al. 2002; 2004, 2007; Gonzalez & Safi-Harb 2003) and radio (Gaensler & Wallace 2003) wavelengths, where the remnant appears as a slightly elliptical shell approximately  $8'$  across.

The X-ray emission from O-rich SNRs, including G292.0+1.8, tends to arise from faster, non-radiative shocks in lower density ejecta and interstellar gas. G292.0+1.8 has a complex X-ray morphology, with widespread shocked circumstellar material superposed on a network of shocked ejecta knots. The SNR also features a filament (or filaments) stretching east-west across the middle of the SNR (commonly called the ‘equatorial belt’ in earlier papers). Analyses of *Chandra* data indicate the equatorial belt is of normal composition, suggesting shocks propagating in circumstellar material (Park et al. 2002, 2004; Gonzalez & Safi-Harb 2003; Lee et al. 2010).

G292.0+1.8 also hosts a pulsar (PSR J1156-5916) with a spin down age of 2900 years (Camilo et al. 2002). The pulsar has been detected over much of the electromagnetic spectrum (see Camilo et al. 2002 for radio observations, Hughes et al. 2003 for X-rays), including 4.5 and 8.0  $\mu\text{m}$  with the IRAC imager on *Spitzer* (Zyuzin et al. 2009). The pulsar wind nebula of PSR J1156-5916 has also been detected in the radio (Gaensler & Wallace 2003), IR (IRAC imagery at 4.5  $\mu\text{m}$  and 8.0  $\mu\text{m}$ ; Zyuzin et al. 2009) and in the X-rays (Hughes et al. 2001). With all these properties and as the second youngest O-rich SNR known in the Galaxy, G292.0+1.8 is an important object for understanding how core-collapse SNRs evolve.

<sup>1</sup> Department of Physics, Astronomy and Geosciences, Towson University, Towson, MD, 21252

<sup>2</sup> Space Telescope Science Institute, 3700 San Martin Drive, Baltimore, MD, 21218

<sup>3</sup> Department of Physics and Astronomy, Johns Hopkins University, 3400 N. Charles Street, Baltimore, MD, 21218

<sup>4</sup> Department of Physics, Box 19059, University of Texas at Arlington, Arlington, TX, 76019

<sup>5</sup> Department of Physics and Astronomy, Dartmouth College, 6127 Wilder Lab, Hanover, NH 037355

<sup>6</sup> Sydney Institute for Astronomy, School of Physics A29, The University of Sydney, NSW 2006, Australia

<sup>7</sup> Department of Physics and Astronomy, Rutgers University, 136 Frelinghuysen Road, Piscataway, NJ, 08854

<sup>8</sup> NASA Ames Research Center, Moffett Field, CA, 94035

<sup>9</sup> Department of Physics, Middlebury College, McCardell Bicentennial Hall 526, Middlebury, VT, 05753

Here we report on a set of imaging observations of G292.0+1.8 obtained with the MIPS and IRS instruments on *Spitzer*. The MIPS 24  $\mu\text{m}$  and 70  $\mu\text{m}$  images trace mostly emission from warm dust heated by shocks in the shocked circumstellar medium (CSM). Our observations also included IRAC imagery at 4.5 and 8.0  $\mu\text{m}$ , though no discernible emission from G292.0+1.8 was detected in these two wavebands (consistent with non-detection at similar wavelengths in the AKARI observations (Lee et al. 2009)). Narrow band images constructed from our IRS spectral maps trace emission from the strongest mid-IR emission lines and provide clues to the location of ejecta within the SNR.

The observations reported here are part of a follow-up to our earlier IRS observations of two positions in G292.0+1.8 (Ghavamian et al. 2009). The spectra obtained earlier showed emission lines from [Ne II]  $\lambda 12.8$ , [Ne III]  $\lambda\lambda 15.5, 36.0$ , [Ne V]  $\lambda 24.3$ , and [O IV]  $\lambda 25.9$ , but no clear evidence of emission from heavier elements. This contrasts with Cas A, where in addition to these lines, IRS spectra showed significant [Ar II]  $\lambda 7.99$ , [Fe II]  $\lambda 17.9$  and [S III]  $\lambda\lambda 18.7, 33.5$  emission (Rho et al. 2008; Smith et al. 2009). Our goal here is to provide a more general description of the SNR as a whole in the mid-IR.

The *Spitzer* observations in this paper complement the existing AKARI study of G292.0+1.8 by Lee et al. (2009) where mid-IR imagery was acquired of the SNR in 10 bands centered at wavelengths ranging from 2.7  $\mu\text{m}$  to 180  $\mu\text{m}$  (including 24  $\mu\text{m}$  band with similar sensitivity and spatial resolution to the MIPS 24  $\mu\text{m}$  images presented here). In addition to the imagery, AKARI spectra were obtained from a section of the belt exhibiting the brightest X-ray emission, as well as the lower portion of the O-rich Spur seen in the [O III] imagery of G292.0+1.8. Our new IRS spectral maps cover the entire SNR over the 5  $\mu\text{m}$  - 36  $\mu\text{m}$  range, providing access to emission lines not covered in the AKARI observations such as [O IV]+[Fe II]  $\lambda 25.9$ , [Ne III]  $\lambda 15.5$   $\mu\text{m}$  (which falls in a gap in AKARI spectral coverage between 13  $\mu\text{m}$  and 18  $\mu\text{m}$ ) and [Si II]  $\lambda 34.8$ . In addition, unlike Lee et al. (2009) who focused on properties of the integrated IR emission from the entire SNR, our analysis includes analysis of shocked CSM in localized regions within G292.0+1.8.

The remainder of this paper is organized as follows: In Section 2, we describe the observations and the techniques used to reduce the data, including the creation of narrow band images from the IRS data. In Section 3, we describe the broad band images and compare them to X-ray and optical images of the SNR. In Section 4, we discuss the emission line images, and discuss these primarily in the context of ejecta from the SNR.

## 2. OBSERVATIONS AND REDUCTIONS

Observations of G292.0+1.8 described here were performed during Cycle 4 of *Spitzer* (PID 40583; P. Ghavamian, PI) and utilized the MIPS (24  $\mu\text{m}$  and 70  $\mu\text{m}$ ) and IRS instruments (Long-Low module only) in mapping mode. The MIPS data were obtained on 2008 March 13 (70  $\mu\text{m}$ ) and 2008 April 15 (24  $\mu\text{m}$ ), while the IRS data were taken on 2008 August 13. The MIPS raster maps at 24  $\mu\text{m}$  and 70  $\mu\text{m}$  covered the entire SNR (8'3 across, or 14 pc at an assumed distance of 6 kpc, Gaensler & Wallace 2003), as well as a sizeable swath of

the surrounding sky. The MIPS 24  $\mu\text{m}$  observations were performed in a one-cycle raster map, with an exposure time of 10 s per pixel and a total integration time of 500 s. The 70  $\mu\text{m}$  observations were also obtained in a one-cycle raster map, with an exposure time of 10s per pixel and total integration time of 380s. The 1- $\sigma$  extended source sensitivity of the MIPS observations was approximately 0.2 MJy sr<sup>-1</sup> at 24  $\mu\text{m}$  and 4 MJy sr<sup>-1</sup> at 70  $\mu\text{m}$ . The MIPS images of G292.0+1.8 are shown in Figure 1.

The IRS spectral maps utilized one cycle of 5 pointings parallel to the LL slit, separated by 120'', along with 112 pointings taken in 6'' steps perpendicular to the slit. Both LL1 (1st order, 19.5-38.0  $\mu\text{m}$ ) and LL2 (2nd order, 14.0-21.3  $\mu\text{m}$ ) were active during the mapping scans, with an exposure time of 32s per pixel (560 individual spectra). The IRS mapping footprint for these observations is shown overlaid onto the MIPS 24  $\mu\text{m}$  image in Figure 2.

### 2.1. Post-Processing of MIPS data

Our MIPS data were processed using calibration pipeline version S18.12.0. MIPS delivers diffraction limited images, so that the relative spatial resolution of any two MIPS channels differs by the ratio of their central wavelengths. To compare the surface brightnesses of features between images, we first degraded the spatial resolution of the 24  $\mu\text{m}$  image to that of the 70  $\mu\text{m}$  image by convolving the former with a PSF kernel using the IDL-based Convolution Kernels software CONVIMAGE (Gordon et al. 2008). We used a PSF kernel appropriate for a 50 K blackbody source. While we do not expect the continuum emission to follow a simple blackbody shape, this temperature is approximately midway between the temperatures of the cold ( $\sim 30$  K) and warm ( $\sim 70$  K) CSM dust components fit to the IRS staring mode spectra of G292.0+1.8 by Ghavamian et al. (2009). After the convolution we used the AIPS (Astronomical Image Processing System)<sup>10</sup> task HGEOM to resample the convolved 24  $\mu\text{m}$  image (2'55 pixel<sup>-1</sup>) onto a grid matching that of the 70  $\mu\text{m}$  image (5'3 pixel<sup>-1</sup>). To extract surface brightness values from selected regions around G292.0+1.8 we utilized the FUNTOOLS package of SAO (<https://www.cfa.harvard.edu/~john/funtools/>).

To compare localized variations in the 70/24 flux ratios with the corresponding X-ray emission in G292.0+1.8, we estimated the X-ray brightnesses using the deep 510 ks *Chandra* image of G292.0+1.8 (Park et al. 2007). We started with the *Chandra* level 1 event file from that observation, processed in the manner described in Park et al. (2007) and filtered over the 0.3-8.0 keV range. Before extracting the X-ray fluxes we blurred the filtered *Chandra* image to the same resolution as the MIPS 24  $\mu\text{m}$  image. The pixel scale of IRAC images is 0'6 pixel<sup>-1</sup>, which is close to the 0'5 pixel<sup>-1</sup> pixel scale of the *Chandra* images. Therefore, we convolved the X-ray image using the CONVIMAGE kernels appropriate for blurring an IRAC 3.6  $\mu\text{m}$  image to MIPS 24  $\mu\text{m}$  resolution. We again used the convolution kernel appropriate for a 50 K blackbody. Finally, we extracted the X-ray counts from individual regions (18 regions were

<sup>10</sup> AIPS is produced and supported by the National Radio Astronomy Observatory, operated by Associated Universities, Inc., under contract with the National Science Foundation

selected, described later in Section 4) in the convolved X-ray image using the FUNCNTS application. We utilized an annular region surrounding G292.0+1.8 in the *Chandra* image to estimate the underlying background level (marked in Figure 3). Although the background region includes a number of faint point sources, their total contribution to the background counts is negligible ( $\lesssim 2\%$ ), so their contribution was not removed before scaling and subtracting the background from each extraction region. After background subtraction, we converted the resulting net counts to count rates by dividing by the exposure time (510 ks). We then converted the count rates to surface brightness using the PIMMS tool from CXC. Note that the X-ray fluxes are estimated without actual spectral modeling, resulting in less accurate flux estimates than would be obtained with spectral models. However, we only seek crude flux estimates for the purpose of identifying systematic trends in the ratios of IR to X-ray emission. Since the fluxes are extracted from CSM shocks, we assumed abundances 0.2 times solar, while taking  $N_H = 6 \times 10^{21} \text{ cm}^{-2}$  and  $kT = 0.75 \text{ keV}$ . These parameters reflect average values for these parameters measured around the rim of G292.0+1.8 by Lee et al. (2010).

### 2.2. Post-Processing of IRS data

We performed our IRS spectral mapping analysis using data processed with *Spitzer* calibration pipeline version S18.7.0. Using the IDL CUBISM software (Smith et al. 2007), we assembled the 560 Basic Calibrated Data files (BCDs) into two data cubes, one for LL1 and one for LL2. The BCDs are heavily affected by hot pixels (especially beyond  $35 \mu\text{m}$ ), which results in vertical columns of elevated pixels in the assembled data cube. To mitigate the effects of these hot pixels, we median smoothed the BCDs prior to creating the data cubes by using the *FILTERIMAGE* routine from the IDL Astronomy User’s library. The smoothing replaces the value of each pixel with the median of the surrounding 3 pixels in a moving box. While this reduces the spatial resolution of the data in the BCDs somewhat, it significantly mitigates the hot pixel columns in the resulting datacube.

The background emission around G292.0+1.8 varies noticeably across the face of the SNR in both MIPS images. At  $24 \mu\text{m}$ , the background is about  $17.6 \text{ MJy sr}^{-1}$  in the northeastern corner of the image in the region used for estimating the background emission in the data cubes. The background rises to a maximum of  $18 \text{ MJy sr}^{-1}$  in the southwestern corner of the image. The corresponding background surface brightnesses in the  $70 \mu\text{m}$  image are  $32 \text{ MJy sr}^{-1}$  and  $35 \text{ MJy sr}^{-1}$ , respectively. This emission gradient can be seen in Figure 1. The variability is due in part to the presence of an H II region along the line of sight just south of G292.0+1.8. It appears as patchy diffuse emission in the narrowband H $\alpha$ , [S II] and [O III] images of the SNR (Winkler & Long 2006).

In the IRS datacubes the H II region along the line of sight to G292.0+1.8 contributes [Ne III]  $\lambda\lambda 15.5, 35.0$ , [S III]  $\lambda\lambda 18.7, 35.0$  and [Si II]  $\lambda 34.8$  line emission, as well as a photo-excited dust continuum starting near  $15 \mu\text{m}$  and slowly rising beyond the edge of the IRS bandpass at  $40 \mu\text{m}$ . The sky spectrum also shows a cluster

of faint, closely spaced emission features between  $15 \mu\text{m}$  and  $20 \mu\text{m}$ . These features are characteristic of PAH emission from the intervening photodissociation regions at  $16.4$  and  $17.0 \mu\text{m}$ , as well as H $_2$  S(1)  $17.1 \mu\text{m}$  emission. At longer wavelengths, faint H $_2$   $28.2 \mu\text{m}$  emission is also detected in the sky spectrum. The excess contribution from this diffuse component, after subtraction of background from the northeastern corner of the datacube, results in residual emission in the datacube when extracting emission line images.

## 3. ANALYSIS

### 3.1. MIPS Imagery

In Figure 1 we present the  $24 \mu\text{m}$  and  $70 \mu\text{m}$  MIPS images of G292.0+1.8. The SNR appears in both bands as an elliptical shell with a banded structure running E-W across its middle, similar to what is observed in the *Chandra* images (Park et al. 2002; 2004; 2007; Lee et al. 2010). For the most part, the morphology and brightness variations of the shell match those seen in the X-rays, with the main difference being the lack of prominent IR emission from X-ray emitting O-rich and Ne-rich ejecta. These results are consistent with continuum emission from circumstellar dust heated by the non-radiative forward shock in G292.0+1.8. Lee et al. (2009) reached the same conclusion based on their AKARI imagery of G292.0+1.8.

Both the Spur and the FMKs can be seen in the  $24 \mu\text{m}$  image, tracing the [O IV]  $\lambda 25.9$  produced by radiative ejecta shocks. The [O IV] emission from these shocks closely follows the distribution of [O III]  $\lambda 5007$  emission observed in narrowband optical imagery (Tuohy, Burton & Clark 1982; Winkler & Long 2006) and optical imaging spectrometry (Ghavamian, Hughes & Williams 2005). In addition, both the Spur (and as we show in Section 3.2.2, the southernmost FMK) exhibit emission from a spectral bump between  $15$  and  $25 \mu\text{m}$  in our IRS spectral maps. This bump (likely a signature of ejecta dust heated in the radiative shocks) also contributes emission to the MIPS  $24 \mu\text{m}$  image of G292.0+1.8.

The flux ratio between IR images at two different wavelengths is sensitive to such parameters as the dust temperature, gas density and dust-to-gas ratio (Dwek 1987). To investigate the global 70/24 flux ratio in G292.0+1.8, we used the FUNCNTS application from FUNTOOLS to integrate the  $24 \mu\text{m}$  and  $70 \mu\text{m}$  emission across the face of G292.0+1.8 (avoiding bright stars within the remnant periphery). We then estimated the total flux and luminosity of the SNR in these bands. We subtracted the sky contribution in each band using an annular region encircling G292.0+1.8 (marked in Figure 3; the same background annulus was used for both the  $24 \mu\text{m}$  and  $70 \mu\text{m}$  images). Similar to the X-ray data, the background annuli in our  $24 \mu\text{m}$  images contain point sources (none are present in the  $70 \mu\text{m}$  images). These point sources contribute  $\lesssim 3\%$  to the total counts in the background regions. After scaling and subtracting the background, the resulting fluxes are  $9.8 \text{ Jy}$  at  $24 \mu\text{m}$  and  $26.4 \text{ Jy}$  at  $70 \mu\text{m}$ , respectively. The globally averaged 70/24 ratio is 2.7, an intermediate value between the local minimum of 1.4 and local maximum of 5.5 reported in Table 1. These fluxes are in good agreement with the two-temperature modified blackbody SED (a mixture of graphite and sil-

icon) calculated by Lee et al. (2009) for a 3000 year old SNR with preshock density of  $0.5 \text{ cm}^{-3}$ . Assuming a distance of 6 kpc to G292.0+1.8 (Gaensler & Wallace 2003), the corresponding luminosities in the MIPS bands are  $L_{24} = 1.9 \times 10^{36} \text{ ergs s}^{-1}$  and  $L_{70} = 1.4 \times 10^{36} \text{ ergs s}^{-1}$  (Note the luminosity at  $24 \mu\text{m}$  includes the contribution of [O IV]+[Fe II] line emission near  $25.9 \mu\text{m}$ ).

Localized variations in the 70/24 flux ratio can be observed both along the shell and throughout the interior of G292.0+1.8. The  $24 \mu\text{m}$  and  $70 \mu\text{m}$  surface brightnesses are shown in Table 1 for a selection of individual regions, along with the corresponding 70/24 ratios. A trend seen in these ratios is that they tend to be largest (i.e., implying coldest dust) along the elliptical outer blast wave of G292.0+1.8. The hottest CSM dust tends to be found along the equatorial belt, though some of the clumpy belt material also extends toward the southwest of the SNR.

A conspicuous difference between the IR and X-ray appearance of G292.0+1.8 is the presence of strong IR emission in parts of the shell lacking X-ray emission. These differences can be seen in Figure 3, where the individual regions have been marked on the MIPS  $24 \mu\text{m}$  and *Chandra* 0.3-8.0 keV images. Regions 6-10 in the southwestern portion of G292.0+1.8 mark clumps where the IR emission in both MIPS images is particularly strong compared to the X-ray emission. The spectral properties of these clumps are clearly different from those of the circumstellar belt (numbered 13-18 in Figure 3) and most of the shell (Regions 1-4 and 11-12). In contrast, sections of the circumstellar belt (Regions 13-18) are prominent both in the MIPS and *Chandra* images. These suggest significant differences between physical conditions in the southwest and those in the rest of the shell and circumstellar belt. X-ray spectra of Regions 13-18 extracted from the 510 ks *Chandra* observation (Park et al. 2007) exhibit no evidence of ejecta (enhanced metal) abundances, and in fact appear fully consistent with cosmic (subsolar) abundances. In addition, the southwestern clumps are not detected in either the [O III] image of G292.0+1.8 (Winkler & Long 2006), nor in [O IV]+[Fe II], [Ne III] or [Si II] in our IRS maps of G292.0+1.8, an indication their emission arises in non-radiative shocks.

## 3.2. Narrowband Maps

### 3.2.1. Emission Line Images

In addition to the IR continuum generated by the shock heated dust in G292.0+1.8, the SNR is also detected in IR forbidden line emission from shocked ejecta. The detected lines were described by Ghavamian et al. (2009), who reported strong O and Ne emission (as well as possible weak S line emission) from the Spur. Clear variations can be seen in the relative fluxes of the ejecta lines in the IRS spectral maps, reflecting variations in physical conditions in the ejecta. To map these variations, we first used CUBISM to extract emission line images from the IRS spectral map.

Due to the presence of underlying dust continuum throughout most of the LL2 and all of the LL1 bandpass, isolating the emission line component required estimation of the continuum level under each line, then the subtraction of this continuum at each position in the datacube. To perform this subtraction, we first used

CUBISM to isolate the continuum emission over a narrow sub-band on either side of the [Ne III]  $\lambda 15.6$  and [O IV]+[Fe II]  $\lambda 25.9$  lines. The corresponding sub-bands used for the [Si II] image were both chosen from continuum on the blue side of  $34.8 \mu\text{m}$  to minimize the impact of hot pixels on the continuum-subtracted [Si II] image.

Collapsing the emission in each of the two bands, we generated two ‘off-band’ images of G292.0+1.8 near each spectral line. We then averaged the two images to approximate an image of the continuum underlying each of the emission lines. We scaled and subtracted this averaged image from that formed by integrating emission from the G292.0+1.8 datacube over each of the O, Ne and Si lines. The scaling factor applied to each background image before subtraction was (1.05,1.0,1.10) for [Ne III], [O IV]+[Fe II], and [Si II] respectively. The wavelength ranges integrated for estimating the underlying [Ne III]  $\lambda 15.5$  continuum in the datacube were  $15.0\text{--}15.2 \mu\text{m}$  and  $15.9\text{--}16.1 \mu\text{m}$ , while that for [O IV]+[Fe II]  $\lambda 25.9$  were  $23.4\text{--}23.9 \mu\text{m}$  and  $26.9\text{--}27.4 \mu\text{m}$ . The corresponding ranges for [Si II]  $\lambda 34.8 \mu\text{m}$  were  $31.4\text{--}32.5 \mu\text{m}$  and  $32.0\text{--}32.7 \mu\text{m}$ . The [Ne V]  $\lambda 24.3$  emission detected in G292.0+1.8 (Ghavamian et al. 2009) was not strong enough to allow creation of useful maps once the nearby continuum was subtracted.

Despite the presence of strong [S III]  $\lambda \lambda 18.7, 33.5$  emission in the datacube, nearly all of this component consisted of unrelated foreground emission (likely from the H II region along the line of sight) as well as photoionized ISM surrounding G292.0+1.8. None of the ejecta in our IRS maps showed significant [S III] emission, although the partially radiative CSM shocks in the equatorial belt of G292.0+1.8 show weak [S III]  $\lambda 18.7$  emission (Figure 6). The presence of weak [S III] from the equatorial belt is consistent with the presence of partially radiative shocks detected in [O III] in the Rutgers Fabry-Perot observations of G292.0+1.8 (Ghavamian, Hughes & Williams 2005).

The [Ne III] and [O IV] emission line maps are shown in Figure 4. The pixel scales of the images are  $5'' \text{ pixel}^{-1}$ , with each image  $11'2 \times 11'2$  square. They bear a strong resemblance to the [O III] optical image (Winkler & Long 2006), indicating that the oxygen and neon originate from the same nucleosynthetic layers within the progenitor. The most prominent O-rich structure, the Spur, is clearly detected in both line maps, while the FMKs seen near the northern and southern edges of G292.0+1.8 in the [O III] images have faint counterparts in [Ne III] and [O IV]. The faint bands of [O III] emission stretching southward from the Spur (the ‘Streamers’) and westward toward the middle of G292.0+1.8 are also detected in the IR. However, there are also some differences between the [Ne III] and [O IV] images. The shape of the Spur differs slightly in the two images, with the [O IV] emission having a somewhat clumpier morphology than the [Ne III] emission. In addition, the FMKs near the southern edge of G292.0+1.8 are more prominent in the [Ne III] images. In particular, the southernmost FMK (an ejecta knot with one of the highest proper motions in G292.0+1.8 (Winkler et al. 2009) and which we name ‘Runaway FMK’) is prominent in the [Ne III] image, but barely detected in [O IV]. This may be due in part to differences in the continuum subtraction between

the two images. Both the sky and SNR continuum just begin to turn on near  $15 \mu\text{m}$ , and increase steadily past  $26 \mu\text{m}$ . Subtraction of this continuum adds more noise to the resulting [O IV] image than to the [Ne III] image in Figure 4, making it more difficult to detect intrinsically faint features such as the FMKs in [O IV].

Summing the emission over all the radiatively shocked ejecta in G292.0+1.8, we find that  $L_{[\text{Ne III}]} \approx 8.2 \times 10^{33}$  ergs  $\text{s}^{-1}$  and  $L_{([\text{O IV}] + [\text{Fe II}])} \approx 2.6 \times 10^{34}$  ergs  $\text{s}^{-1}$ , assuming a distance of 6 kpc. The [O IV]+[Fe II] luminosity of G292.0+1.8 (which should be close to the intrinsic value due to the minimal impact of interstellar reddening at  $25 \mu\text{m}$ ) is approximately six times lower than the unreddened [O III] luminosity ( $1.6 \times 10^{35} d_6^2$  ergs  $\text{s}^{-1}$ ) reported by Winkler & Long (2006). On the other hand, the [Si II]  $\lambda 34.8$  emission map shows no emission from the Spur. Save for the belt of O-rich material running westward from the Spur (not to be mistaken with the circumstellar belt seen in X-rays), none of the radiatively shocked O-rich ejecta produce significant [Si II] emission. The only feature clearly visible in the [Si II] image in Figure 4 is a blob of emission located just interior to the Spur. Although the [Si II] image is considerably noisier than the [Ne III] and [O IV] images and suffers from fixed pattern residuals leftover from the hot pixel interpolation, it is evident that there is no substantial [Si II] emission from the radiatively shocked, optically bright ejecta in G292.0+1.8.

### 3.2.2. 15-25 $\mu\text{m}$ Continuum Emission

The ability to generate images of G292.0+1.8 in isolated spectral ranges from our IRS maps allows us to isolate regions of pure continuum emission to search for emission from shock-heated ejecta dust. In our earlier spectroscopic study of G292.0+1.8 (Ghavamian et al. 2009) we identified a broad bump of emission arising from the lower section of the O-rich Spur and centered near  $18 \mu\text{m}$  and extending from  $15 \mu\text{m}$  to  $25 \mu\text{m}$ . Aside from this prominent bump, the only other observed spectral features from the Spur were emission lines. The spectral bump is a possible signature of protosilicate dust emission from  $\text{Mg}_2\text{SiO}_4$  or  $\text{MgSiO}_3$ , and has been detected in *Spitzer* IRS maps of 1E0102–72.3 (Sandstrom et al. 2009; Rho et al. 2009) and Cas A (Rho et al. 2008; Smith et al. 2009). Detection of the 15-25  $\mu\text{m}$  bump in G292.0+1.8 could be evidence that dust formed in the SN ejecta, and that this dust is currently being heated in the radiative ejecta shocks. However, given the complicated mixture of the shocked and photoionized CSM (as well as unrelated foreground emission from the nearby H II region) overlying the Spur in G292.0+1.8, we sought to confirm the spatial coincidence of the emission bump with the supernova ejecta.

To this end, we used CUBISM to subtract the line of sight background from the datacube using emission off the eastern edge of G292.0+1.8 (we used sky in this region because it is closest to the Spur). We then integrated the emission between  $15 \mu\text{m}$  and  $25 \mu\text{m}$  from our IRS LL2 datacube of G292.0+1.8, while excluding the [Ne III]  $\lambda 15.5$  line emission from the ejecta in this bandpass. Although there is no evidence of significant [S III]  $\lambda 18.7$  emission from the ejecta, we excluded this emission line as well during the integration. This sky-subtracted

continuum image of G292.0+1.8 in the 15-25  $\mu\text{m}$  range is shown in the lower right panel of Figure 4.

The 15-25  $\mu\text{m}$  map shows extensive continuum emission from G292.0+1.8, arising almost entirely from shock-heated CSM dust. The equatorial belt and southwestern regions (e.g., Regions 13-16 and 6-10) are especially prominent, while the lower density filaments along the elliptical shell (e.g., regions 1,2,11 and 12 from Figure 3) are fainter. These trends are consistent with the dust temperature variations reflected in the 70/24 flux ratio. The continuum from most of the CSM shocks begins near  $15 \mu\text{m}$ , then rises steadily past the red end of the IRS bandpass at  $36 \mu\text{m}$ . Remarkably, however, some of the radiatively shocked O-rich ejecta (such as the Spur) are also detected in the 15-25  $\mu\text{m}$  map. The Runaway FMK (marked by a red arrow at the bottom of each panel in Figure 4), which has been thrown clear of most of the shocked CSM in the interior of G292.0+1.8, can also be seen. The knot is located in a region of lower, less complicated background emission, allowing the emission from this knot to stand out more easily than for the other FMKs lying in the projected interior. The detection of 15-25  $\mu\text{m}$  IR continuum from both the Spur and the Runaway FMK is strong evidence that whether the emission arises from a 15-25  $\mu\text{m}$  ‘bump’ or some other type of emission feature, dust grains most likely formed in the O-rich ejecta and are currently being heated by radiative shocks.

## 4. DISCUSSION

### 4.1. MIPS 70/24 ratios

The effective temperatures of heated interstellar dust grains in SNRs are largely dependent on the post shock gas density (Dwek 1987; Dwek, Foster & Vancura 1996), and hence, by extension, on the preshock gas density. At the high gas temperatures encountered in young non-radiative SNRs, the impact of electrons from the hot postshock plasma is the primary source of dust heating. On the other hand, dust sputtering in these shocks is primarily caused by proton impacts. At these high temperatures, the amount of energy deposited per electron impact into the dust grains is approximately constant, so that the equilibrium dust temperature (and hence IR emissivity) of the dust depends mainly on the electron (and hence gas) density (e.g., Figure 6b from Dwek 1987 and Figure 8 from Dwek, Foster & Vancura 1996). Assuming similar gas temperatures, compositions and column densities in the CSM shocks (consistent with the X-ray spectral fits of Lee et al. (2010)), regions with bright X-ray emission should broadly correlate with regions of high gas density, which in turn correlate with regions having bright IR emission and high dust temperatures. The brightest X-ray emission should then correspond to IR emission with the smallest 70/24 flux ratios.

Comparing the MIPS and *Chandra* X-ray images of G292.0+1.8, we find that there does appear to be a correlation between the 24  $\mu\text{m}$  and 70  $\mu\text{m}$  surface brightnesses and the X-ray surface brightness for most of the CSM shocks in G292.0+1.8. Interestingly, however, there are departures from this relationship observed along the southwestern side of G292.0+1.8. Specifically, the surface brightnesses of the southwestern CSM clumps (corresponding to Regions 6-10 in Figure 3) are  $\sim 3$  times

higher than the rest of the shell in both IR bands, yet their X-ray counterparts are either faint or almost non-existent. The lack of bright X-ray emission matching the bright IR clumps in the SW is not due to enhanced local absorption of X-rays, since Lee et al. (2010) did not find a large enough variation in column density ( $5 \times 10^{21} \lesssim N_H \lesssim 7 \times 10^{21}$ ) around the rim to account for the reduced X-ray flux in the SW corner of G292.0+1.8.

To quantify the relationships described above, we plotted the 24  $\mu\text{m}$  and 70  $\mu\text{m}$  surface brightnesses of the selected regions in G292.0+1.8 against the X-ray surface brightnesses of those regions in Figure 5 (top panel). The 70/24 ratios (which are plotted against the X-ray surface brightnesses in the lower panel of Figure 5) show a noticeable declining trend with increasing X-ray emission, consistent with our prediction. One caveat to consider when interpreting Figure 5 is that X-ray emission from the ejecta overlies the emission from some of the CSM shocks. Therefore, the X-ray count rates in some of the CSM regions plotted in Figure 5 are over-estimated to various degrees (save for Region 4, most of the regions contain little or no discernible emission from ejecta). The ejecta contribution to the region counts is likely to add scatter to the values along the horizontal axis of the plot. However, the plot is still useful for identifying systematic trends between the IR and X-ray properties of G292.0+1.8, and they clearly demonstrate a relationship between emission in the two bands. The 70  $\mu\text{m}$  fluxes show more scatter than the 24  $\mu\text{m}$  fluxes and their distribution appears somewhat flatter than the 24  $\mu\text{m}$  when plotted versus X-ray surface brightness. Dividing the two fluxes results in a more distinct correlation, with the 70/24 ratio declining with X-ray surface brightness.

The trend between the 70/24 ratio and the X-ray surface brightness is also consistent with predictions from the shock models of Dwek, Foster & Vancura (1996). Specifically, the lowest ratios ( $\sim 1.5$ -1.8) are found in the denser material of the equatorial belt, while the largest ratios ( $\sim 2.5$ -5) are found in the low density, fainter sections of the outer shell. A more quantitative comparison can be made with the Dwek, Foster & Vancura (1996) predictions by using dust spectra for their  $800 \text{ km s}^{-1}$  shock models (this shock speed gives a temperature closest to the average of the temperatures of the different regions measured by Lee et al. (2010)). From Figure 8c of Dwek, Foster & Vancura (1996), the dust spectra for preshock gas densities of  $0.1 \text{ cm}^{-3}$  and  $1.0 \text{ cm}^{-3}$  should be most appropriate for modeling the IR emission from the equatorial belt and circumstellar shell in G292.0+1.8, respectively. The dust spectra from Dwek, Foster & Vancura (1996) predict  $\nu_{70} F(70)/\nu_{24} F(24) \approx 2.3$  for  $n = 0.1 \text{ cm}^{-3}$  and  $\nu_{70} F(70)/\nu_{24} F(24) \approx 0.7$  for  $n = 1 \text{ cm}^{-3}$ . The predicted flux ratios are then  $F(70)/F(24) \approx 6.7$  for  $n = 0.1 \text{ cm}^{-3}$  and  $F(70)/F(24) \approx 2$  for  $n = 1 \text{ cm}^{-3}$ . These compare favorably with the observed ratios for the equatorial belt and outer shell in Table 1, though the observed ratios for the shell are somewhat lower than predicted. This is likely due to the inferred preshock density of the shell obtained by Lee et al. (2010) ( $\sim 0.3$ - $0.5 \text{ cm}^{-3}$ ) being slightly larger than that of the  $n = 0.1 \text{ cm}^{-3}$  model of Dwek, Foster & Vancura (1996).

Overall, the regions with the hottest dust in Figure 5 are (not suprisingly) Regions 15, 17 and 18, correspond-

ing to the brightest clumps in the *Chandra* image of G292.0+1.8. Park et al. (2002) found that the equatorial belt (Region 15) had a higher density and slightly lower temperature than the outer shell of G292.0+1.8, while Ghavamian, Hughes & Williams (2005) detected faint [O III]  $\lambda 5007$  emission from the belt. This indicates that the elevated density in the equatorial belt in Region 15 has caused the shocks to become partially radiative at that location. The elliptical shell surrounding G292.0+1.8, where the blast wave propagates through the relic red supergiant (RSG) wind (Lee et al. 2010), has the lowest preshock gas densities, and hence the coldest shocked CSM dust.

Figure 5 provides an important clue to the origin of the elevated IR to X-ray flux ratios in the southwestern portion of G292.0+1.8. Although the emission in the southwest is bright in both MIPS images, the 70/24 ratios from this part of G292.0+1.8 (as reflected in the 70/24 ratios for the CSM knots in Regions 6-10) are similar to those of the equatorial belt, where emission is bright in both IR and X-rays. This suggests that the dust is just as hot in the southwestern CSM knots as they are in the belt (as reflected in the 70/24 ratios for Regions 13-18). This in turn implies that the gas densities in the southwest and in the equatorial belt are similar. Therefore, the most likely explanation the anomalously high IR to X-ray ratios of Regions 6, 7, 9 and 10 is that these clumps have higher dust-to-gas ratios than the clumps in the equatorial belt. A localized, elevated dust content in the southwest of G292.0+1.8 may indicate that the dust in this portion of the SNR is not well coupled to the X-ray emitting gas, or it may reflect variations in the dust condensation efficiency in the relic red giant wind of the progenitor. Even allowing for variations in dust content around the rim of G292.0+1.8, the average dust-to-gas ratio inferred by Lee et al. (2009) for this SNR ( $\sim 10^{-3}$ ) is significantly lower than the average Galactic value (Weingartner & Draine 2001).

In Figure 6 we show sample IRS mapping spectra extracted from four of the regions marked in Figure 3 (Regions 4, 7, 15 and 17). The spectra were obtained from a section of the blast wave in the NW (Region 4), a knot of bright IR emission in the SW (Region 7), the brightest section of the equatorial belt (Region 15) and a large clump just above the eastern edge of the equatorial belt. We subtracted the same background emission from all four of the IRS spectra after averaging the emission from two sky regions located just off the eastern and western sides of G292.0+1.8 (marked by the cyan boxes in the left panel of Figure 3).

The background-subtracted spectra from the four regions described above are dominated by a rising dust continuum. The blast wave emission from Region 4 shows a slowly rising continuum which starts near 15  $\mu\text{m}$  and rises past the red end of the IRS bandpass. In contrast, the clump in Region 7 shows a brighter, more steeply rising dust continuum which peaks at a shorter wavelength than Region 4 (at approximately 33  $\mu\text{m}$ ). This is consistent (based on the discussion in Section 4.1) with a higher overall density in region 7 than Region 4. Region 15, while showing a prominent dust continuum, also exhibits faint emission lines of [Ne III]  $\lambda 15.5$ , [O IV]+[Fe II]  $\lambda 25.9$ , [S III]  $\lambda 18.7$  and [Si II]  $\lambda 34.8$ . Region 15 has

been detected in [O III] in the optical (Ghavamian et al. 2005), and was shown by Park et al. (2002) to be both denser and cooler than the blast wave filaments encircling G292.0+1.8. The shocks in the equatorial belt have formed partial cooling zones and hence are partially radiative, giving rise to the observed faint IR (and optical) line emission. The continuum from Region 17 is similar to that of Region 15, indicating similar dust temperature. The presence of faint [Ne III]  $\lambda$ 15.5 and [O IV]+[Fe II]  $\lambda$ 25.9 in the spectrum of Region 17 indicates that the shocks in this clump have also started to form radiative cooling zones.

#### 4.2. The [Si II] emission and the thermodynamic state of the ejecta

In their analysis of the 510 ks *Chandra* image of G292.0+1.8, Park et al. (2007) concluded that the thermodynamic state of the ejecta (as reflected by temperature, density and ionization state) exhibits a significant gradient between the southeastern and northwestern sides of G292.0+1.8. The X-ray hardness ratios they obtained from the *Chandra* data indicated a substantially lower temperature for the SE ( $kT \sim 0.7$  keV) than the W and NW ( $kT \sim 5$  keV). This is consistent with the fact that most of the optical and IR-emitting SN ejecta – the Spur and its associated streamers – are found in the SE of G292.0+1.8. The ejecta shocks in the rest of the SNR, by contrast, are mostly still in the non-radiative phase.

The trends described above can be seen in the narrowband X-ray images of G292.0+1.8 in O He  $\alpha$  and Ne He  $\alpha$  (Park et al. 2007). These images show a strong spatial correlation with the optical [O III] and IR [Ne III] and [O IV] emission in the SE. In contrast, the narrowband X-ray images in Si He  $\alpha$  (which traces hotter gas than O Ly  $\alpha$  and Ne He  $\alpha$  owing to its higher nuclear charge) is almost entirely absent in the SE. The lack of Si emission from the SE in both the X-rays and the IR (save for the isolated [Si II] ejecta blob in Figure 4) indicates that the reverse shock has not yet encountered most of the Si-rich ejecta in the SE. Park et al. (2007) speculated that the cooler thermodynamic state of the ejecta in the SE of G292.0+1.8 was the result of an asymmetric supernova explosion, where less energy was channeled into that direction than the rest of the SNR. The lack of extensive [Si II]  $\lambda$ 34.8 emission in the SE of G292.0+1.8 may indicate that the SNR is less evolved in that direction, providing further evidence in favor of the asymmetric explosion picture.

#### 4.3. 15-25 $\mu$ m Bump

As shown in Figure 4, the O-rich Spur and the Runaway FMK in G292.0+1.8 are detected in the 15-25  $\mu$ m continuum image extracted from the *Spitzer* IRS datcube of G292.0+1.8. The presence of such continuum indicates that dust grains exist within the ejecta. To investigate this possibility further, we extracted IRS spectra of the Runaway FMK, using a circular region centered on the knot. We subtracted sky emission using an identically sized region located approximately  $10''$  radially inward from the FMK (marked by the small cyan circle in Figure 3). The resulting spectrum is shown in Figure 7. The sky spectrum shows emission features from intervening photodissociation region (PDR) and H II regions

along the line of sight to G292.0+1.8: PAH emission at 16.4 and 17.0  $\mu$ m, as well as H<sub>2</sub> S(1) 17.1  $\mu$ m and H<sub>2</sub> 28.2  $\mu$ m emission. Line of sight emission from [Ne III]  $\lambda$ 15.5, [Si II]  $\lambda$ 18.7, 33.5, [Fe II]+[O IV]  $\lambda$ 25.9 and [Si II]  $\lambda$ 34.8 are also present, as is continuum emission from photoheated dust. After subtraction of the background, both [Ne III] and [Fe II]+[O IV] emission remain, signatures of the O- and Ne-rich ejecta. However, the 15-25  $\mu$ m bump also remains. The spectral characteristics of this feature are very similar to those of the Spur (Ghavamian et al. 2009), and similar to what is seen in the radiatively shocked O-rich ejecta of 1E0102–72.3 (Sandstrom et al. 2009; Rho et al. 2009). This strengthens the case for SN dust (Mg<sub>2</sub>SiO<sub>4</sub>/MgSiO<sub>3</sub>) in the ejecta of G292.0+1.8. It also dispels the possibility raised by Lee et al. (2009) that oversubtraction of the overlying dust continuum was responsible for the lack of significant 24-36  $\mu$ m continuum emission in our earlier IRS spectrum of the Spur (Ghavamian et al. 2009).

#### 4.4. The Narrow Tail

The elongated structure extending southward of G292.0+1.8 in the 24  $\mu$ m and 70  $\mu$ m images exhibits a very interesting morphology. It was first noted by Lee et al. (2009) in their AKARI observations of G292.0+1.8, who referred to feature as a ‘Narrow Tail’. It appears to be connected to the streamers of O-rich ejecta extending south of the Spur (seen in the [O III] image in Figure 1, and in the 24  $\mu$ m MIPS image). However, the Narrow Tail has no X-ray counterpart, and no corresponding optical emission. The 70/24 ratio (Region 19 in Table 1) is 4.2, which indicates cold dust. The background-subtracted IRS spectrum of the Narrow Tail is shown in the right panel of Figure 7. The location used for the estimating the background contribution to the Narrow Tail spectrum is marked by the elongated cyan region in Figure 3. The spectrum of the Narrow Tail in Figure 7 is consistent with cold dust – it peaks beyond the IRS bandpass. These colors are similar to IR cirrus, rather than dust heated by UV from the core collapse explosion. Dwek & Arendt (2008) presented an analysis of light echoes near Cas A, and found that the 70/24 ratios of these echoes was significantly smaller than seen in normal IR cirrus, an indication that the dust had been significantly heated. Dwek et al. found that graphite dust was required to explain the emission, finding that the dust temperature ( $\sim 175$  K) indicated very strong heating from incident UV radiation, rather than optical photons from the SN. In the case of G292.0+1.8, the colors of the elongated structure indicate much colder dust ( $\lesssim 25$  K), hence heating by UV emission from the SN that produced G292.0+1.8 is highly unlikely. There is weak [Si II]  $\lambda$ 34.8 emission from the sky-subtracted spectrum of the Narrow Tail, as well as faint [Fe II]+[O IV] and a hint of H<sub>2</sub> S(0,0) at 28.2  $\mu$ m. This is all consistent with a clump of cold interstellar cloud material (IR cirrus) which has been heated by ambient stellar UV light. We conclude that despite the very suggestive morphology and alignment of this feature with the streamers of O-rich material emanating from the Spur, it appears to be a chance alignment between an interstellar cloud and the elongation axis of the O-rich streamers.

We have presented MIPS 24  $\mu\text{m}$  and 70  $\mu\text{m}$  imaging and IRS spectral mapping of G292.0+1.8 obtained with *Spitzer*. These observations complement the existing AKARI study of G292.0+1.8 (Lee et al. 2009). Our results are as follows:

1. The MIPS data show that most of the filaments seen in the X-rays along the periphery of the SNR, as well as the band of equatorial material stretching across its middle, emit dust continuum emission in the mid-IR. The IRS mapping data of the filaments and clumps show broad-band, rising continua between 15  $\mu\text{m}$  and 40  $\mu\text{m}$ , a clear signature of shock-heated dust. The shapes of the dust continua are consistent with a mixture of graphite and silicate dust, as is observed in the non-radiative blast waves of other SNRs (e.g., Williams et al. 2011).

2. The MIPS 70/24 flux ratio varies significantly ( $1.5 \lesssim F_{70}/F_{24} \lesssim 5$ ) between the blast wave, equatorial belt and the southwestern clumps. These variations primarily reflect differences in dust temperature around G292.0+1.8, and plots of the 70/24 ratio versus X-ray surface brightness are consistent with variations in CSM density inferred from X-ray observations (Lee et al. 2010). The 70/24  $\mu\text{m}$  ratios are also consistent with predictions from dusty shock models (Dwek, Foster & Vancura 1996) with shock speeds and preshock densities matching those predicted by the X-ray observations of Lee et al. (2010).

3. No mid-IR emission (either lines or continuum) is detected from the non-radiative, X-ray emitting ejecta seen in the *Chandra* images G292.0+1.8. The radiatively shocked O-rich ejecta are detected in the MIPS 24  $\mu\text{m}$  image, with most of the ejecta emission in that band consisting of [O IV]+[Fe II]  $\lambda$ 25.9 emission. Us-

ing an isolated FMK located near the southern edge of G292.0+1.8 we have confirmed the detection of the 15-25  $\mu\text{m}$  emission bump from the radiatively shocked O-rich ejecta (possibly  $\text{Mg}_2\text{SiO}_4$  or  $\text{MgSiO}_3$  dust formed in the ejecta).

4. Continuum-subtracted emission line maps of the [Ne III]  $\lambda$ 15.5 and [O IV]+[Fe II]  $\lambda$ 25.9 emission show a strong spatial correlation between the two, and emission in these lines is detected from both the Spur and the FMKs. However, neither of these two structures is detected in the continuum-subtracted [Si II]  $\lambda$ 34.8 maps of G292.0+1.8. Save for a localized blob of [Si II] emission near the inner edge of the Spur, no obvious emission from this species is seen elsewhere in the SNR. Since the entire southeastern portion of G292.0+1.8 is also deficient in Si line emission in the X-rays (Park et al. 2007), the lack of both IR and X-ray emission from Si in the Spur indicates that most of the Si is unshocked in the southeastern quadrant of G292.0+1.8 and that save for the [Si II]-emitting blob, the reverse shock has not yet penetrated most of the Si-rich ejecta in the southeast. This may indicate that the southeastern portion of G292.0+1.8 is less evolved than the rest of the SNR, and may be further evidence of the asymmetric explosion scenario proposed by Park et al. (2007).

This work is based on observations made with the *Spitzer Space Telescope*, which is operated by the Jet Propulsion Laboratory, California Institute of Technology under a contract with NASA. Support for the work of P. G. was supported by NASA through the *Spitzer* Guest Observer Program, as well as HST Grant GO-10916.08. P. F. W. acknowledges support from the NSF through Grant AST-0908566.

## REFERENCES

- Camilo, F., et al. 2002, ApJ, 567, L71  
 Clark, D., Tuohy, I. & Becker, R. 1980, MNRAS, 193, 129  
 Dwek, E. 1987, ApJ, 322, 812  
 Dwek, E. & Arendt, G. R. 2008, ApJ, 685, 976  
 Dwek, E., Foster, S. M. & Vancura, O. 1996, ApJ, 457, 244  
 Gaensler, B. M., & Wallace, B. J. 2003, ApJ, 594, 326  
 Ghavamian, P., Hughes, J. P., & Williams, T. B. 2005, ApJ, 635, 365  
 Ghavamian, P., Raymond, J. C., Blair, W. P., Long, K. S., Tappe, A., Park, S. & Winkler, P. F. 2009, ApJ, 696, 1307  
 Gonzalez, M., & Safi-Harb, S. 2003, ApJ, 583, L91  
 Gordon, K., Engelbracht, C. W., Rieke, G. H., Misselt, K. A., Smith, J.-D. T. & Kennicutt, R. C. 2008, ApJ, 682, 336  
 Goss, W. M., Shaver, P. A., Zealey, W. J., Murdin, P. & Clark, D. H. 1979, MNRAS, 188, 357  
 Hughes, J. P., Slane, P. O., Burrows, D. N., Garmire, G., Nousek, J. A., Olbert, C. M. & Keohane, J. W. 2001, ApJ, 559, L153  
 Hughes, J. P., Slane, P. O., Park, S., Roming, P. W. A. & Burrows, D. N. 2003, ApJ, 591, L139  
 Lee, H.-G., et al. 2009, ApJ, 706, 441  
 Lee, J.-J., Park, S., Hughes, J. P., Slane, P. O., Gaensler, B. M., Ghavamian, P. & Burrows, D. N. 2010, ApJ, 711, 861  
 Park, S., et al. 2002, ApJ, 564, L39  
 Park, S., et al. 2004, ApJ 602, L33  
 Park, S., et al. 2007, ApJ 670, L121  
 Rho, J. H., et al. 2008, ApJ, 673, 271  
 Rho, J. H., Reach, W. T., Tappe, A., Hwang, U., Slavin, J. D., Kozasa, T. & Dunne, L. 2009, ApJ, 700, 579  
 Sandstrom, K. M., Bolatto, A. D., Stanimirovic, S., van Loon, J. Th., & Smith, J. D. T. 2009, ApJ, 696, 2138  
 Smith, J. D. T., et al. 2007, PASP, 119, 1133  
 Smith, J. D. T., Rudnick, L., DeLaney, T., Rho, J., Gomez, H., Kozasa, T., Reach, W. & Isensee, K. et al. 2009, ApJ, 693, 713  
 Tuohy, I. R., Burton, W. M. & Clark, D. H. 1982, ApJ, 260, L65  
 Weingartner, J. & Draine, B. 2001, ApJ, 548, 296  
 Williams, B. J. et al. 2011, ApJ, 729, 65  
 Winkler, P. F., & Long, K. S. 2006, AJ, 132, 360  
 Winkler, P. F., Twelker, K., Reith, C. N. & Long, K. S. 2009, ApJ, 692, 1489  
 Zyuzin, D. A., Danilenko, A. A., Zharikov, S. V. & Shibanov, Yu. A. 2009, A&A, 508, 855



TABLE 1  
 SURFACE BRIGHTNESSES OF FEATURES IN MIPS 24  $\mu\text{M}$  AND 70  $\mu\text{M}$  IMAGES OF G292.0+1.8

Region Number	F(24) (MJy sr $^{-1}$ )	F(70) (MJy sr $^{-1}$ )	$\frac{F(70)}{F(24)}$
1	0.74 $\pm$ 0.36	3.79 $\pm$ 0.83	5.14 $\pm$ 2.73
2	1.68 $\pm$ 0.25	6.68 $\pm$ 0.57	3.98 $\pm$ 0.68
3	3.91 $\pm$ 0.36	10.4 $\pm$ 0.84	2.65 $\pm$ 0.32
4	1.93 $\pm$ 0.28	6.77 $\pm$ 0.65	3.50 $\pm$ 0.61
5	3.03 $\pm$ 0.39	10.5 $\pm$ 0.91	3.48 $\pm$ 0.54
6	6.47 $\pm$ 0.84	14.4 $\pm$ 1.85	2.23 $\pm$ 0.41
7	8.40 $\pm$ 0.97	17.4 $\pm$ 2.15	2.07 $\pm$ 0.35
8	2.79 $\pm$ 0.59	8.20 $\pm$ 1.38	2.94 $\pm$ 0.79
9	6.13 $\pm$ 0.64	16.4 $\pm$ 1.87	2.68 $\pm$ 0.38
10	5.62 $\pm$ 0.64	14.2 $\pm$ 1.47	2.52 $\pm$ 0.39
11	2.35 $\pm$ 0.24	7.62 $\pm$ 0.57	3.24 $\pm$ 0.41
12	2.12 $\pm$ 0.38	6.91 $\pm$ 0.87	3.26 $\pm$ 0.72
13	5.05 $\pm$ 0.72	11.1 $\pm$ 1.62	2.20 $\pm$ 0.45
14	5.05 $\pm$ 0.64	9.24 $\pm$ 1.33	1.83 $\pm$ 0.35
15	7.58 $\pm$ 0.53	12.2 $\pm$ 1.20	1.61 $\pm$ 0.19
16	5.80 $\pm$ 0.34	10.7 $\pm$ 0.76	1.84 $\pm$ 0.17
17	6.38 $\pm$ 0.44	8.79 $\pm$ 0.96	1.38 $\pm$ 0.18
18	3.18 $\pm$ 0.54	4.88 $\pm$ 1.19	1.54 $\pm$ 0.46
19	0.39 $\pm$ 0.19	1.67 $\pm$ 0.44	4.24 $\pm$ 2.34

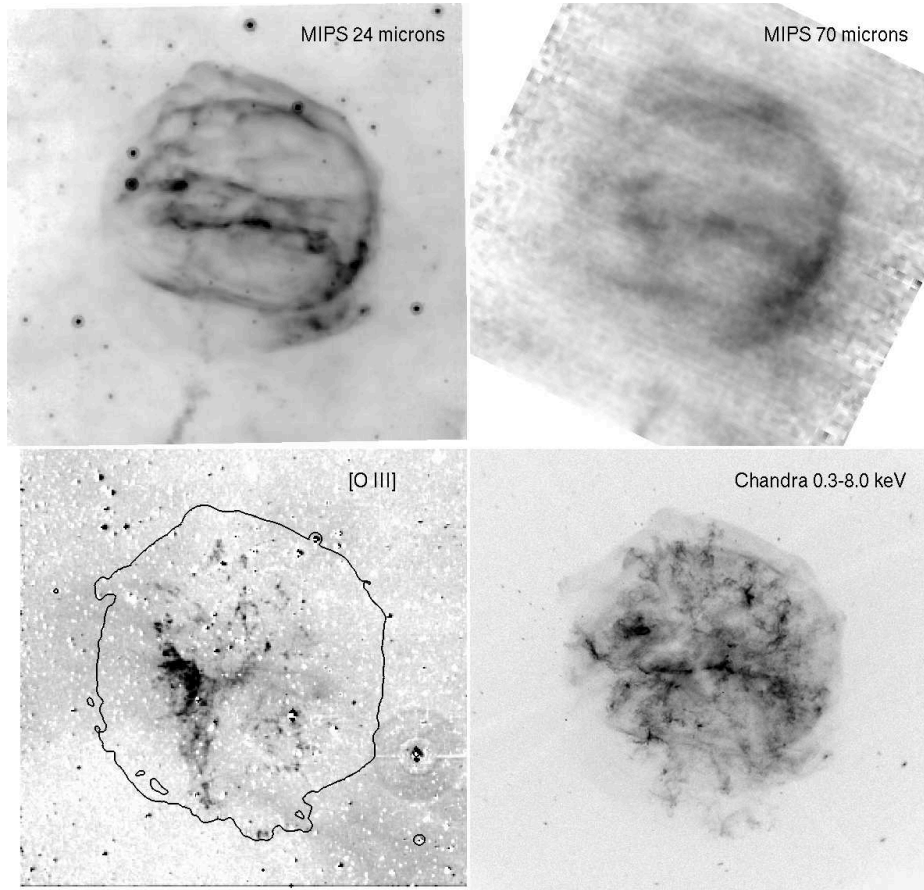


FIG. 1.— MIPS images of G292.0+1.8, shown alongside the optical [O III] image (Winkler & Long 2006) and the 510 ks *Chandra* X-ray image (Park et al. 2007). The outermost X-ray contour from the *Chandra* image is marked on the [O III] image. Each image is  $12'.7 \times 13'.4$  across, with East located at the left and North at the top. The emission in the  $24 \mu\text{m}$  and  $70 \mu\text{m}$  images is predominantly produced by shock-heated circumstellar dust. The O-rich ‘Spur’ is the bright, crescent-shaped feature to the left of center in the [O III] image. The ‘Streamers’ are the fainter fingers of emission stretching southward from the Spur. The fast-moving knots (FMKs) are the small knots of emission seen above and below the center of the [O III] image. A faint elongated feature (named ‘the Narrow Tail’ in Lee et al. 2009) in the south of G292.0+1.8 can be seen near the bottom of the two MIPS images. The Narrow Tail has no counterpart in the [O III] or X-ray images.

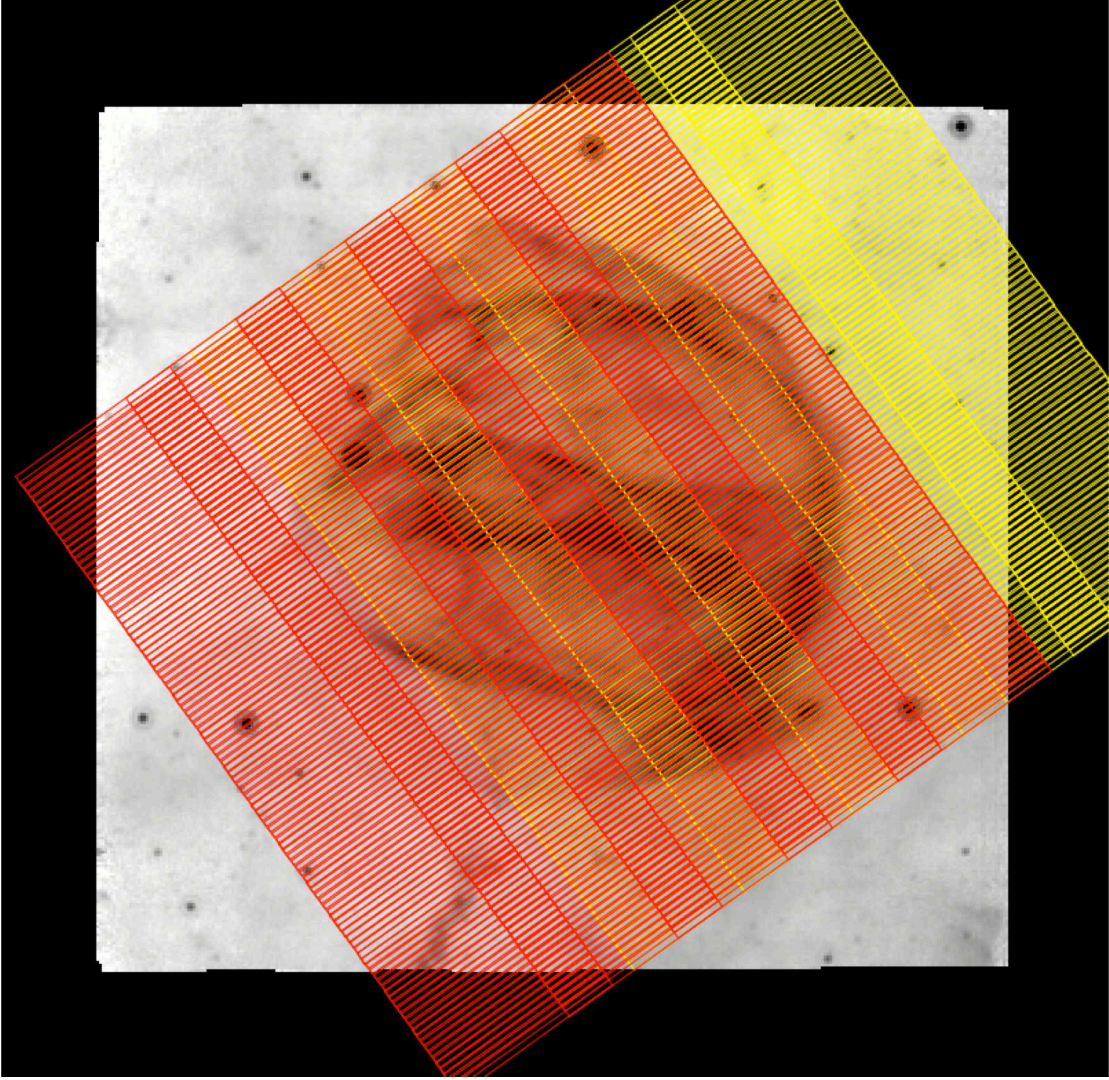


FIG. 2.— The IRS spectral mapping footprint, overlaid onto the MIPS  $24\ \mu\text{m}$  image of G292.0+1.8 for the date of the IRS observations. Long-Low 2 ( $14.2\text{--}21.8\ \mu\text{m}$ ) slit positions are marked in yellow, and Long-Low 1 ( $20.6\text{--}40\ \mu\text{m}$ ) are marked in red. Slits are  $10''.5 \times 168''$  in size.

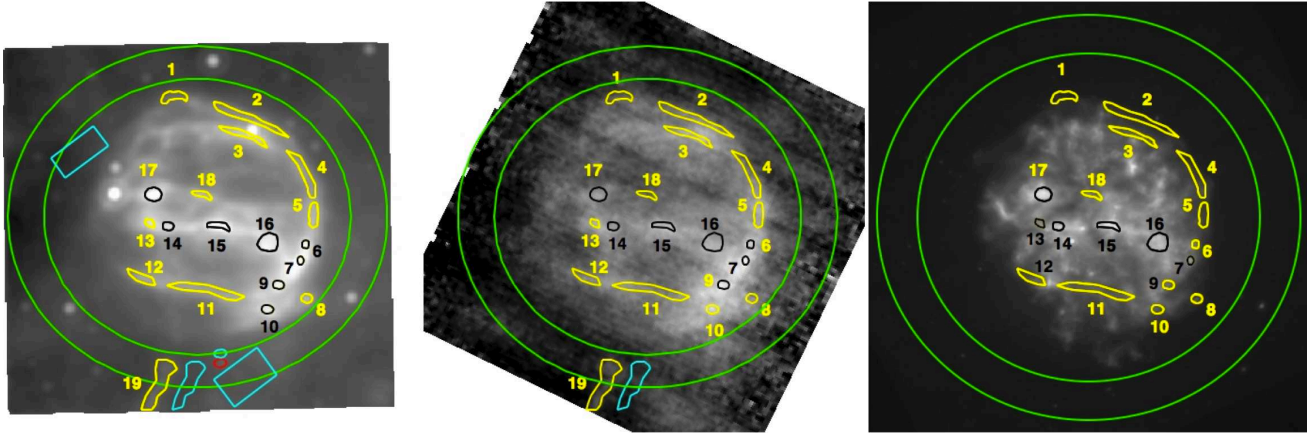


FIG. 3.— Left: The  $24\ \mu\text{m}$  MIPS image of G292.0+1.8, shown with the flux extraction regions from Table 1 marked. The image has been convolved with a PSF kernel to match the  $70\ \mu\text{m}$  PSF of MIPS. Middle: the  $70\ \mu\text{m}$  MIPS image with the flux extraction regions marked. Right: The 510 ks *Chandra* ACIS image of G292.0+1.8, blocked to  $1''$  pixels and convolved with the MIPS  $24\ \mu\text{m}$  PSF, also with the Table 1 extraction regions marked. This image is used in computing the X-ray fluxes shown in Figure 5. Region 19 (corresponding to the Narrow Tail) exhibits no discernible X-ray emission, so is omitted in the X-ray flux measurements. The red circular region on the  $24\ \mu\text{m}$  image marks the extraction box for the Runaway FMK spectrum shown in Figure 7. The green annuli marked around the SNR are used for estimating and subtracting the background emission in each extraction region. Although the background annuli include a few point sources, these objects contribute negligibly to the summed background counts. The background used for generating the IRS spectra in Figure 6 was estimated by averaging the emission in the two cyan boxes shown in the left panel. The elongated and circular cyan regions were used for estimating the background emission for the IRS spectra of the Narrow Tail and Runaway FMK, respectively, in Figure 7. Some regions are colored in black to create better contrast from the surrounding emission.



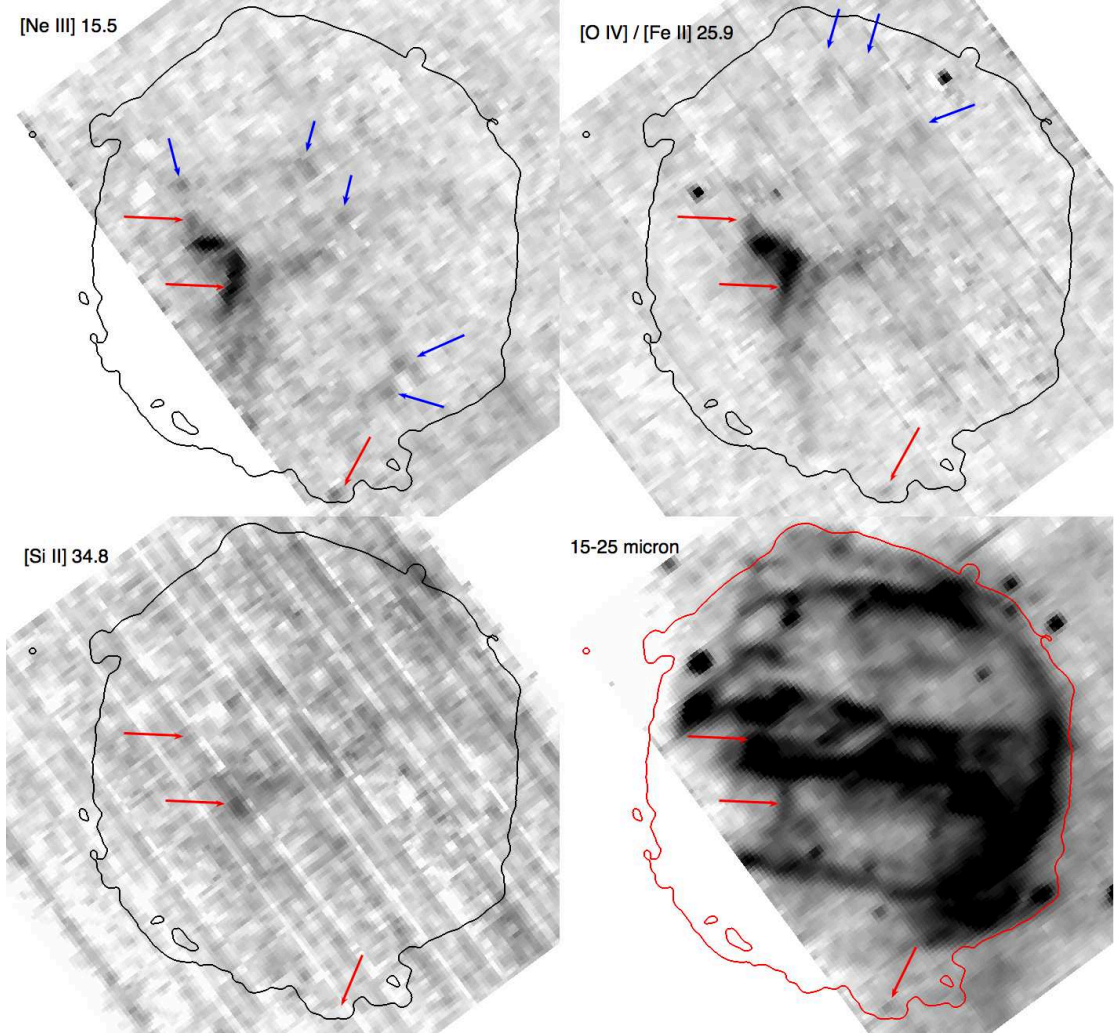


FIG. 4.— Images of G292.0+1.8 in  $[\text{Ne III}] \lambda 15.5$ ,  $[\text{O IV}] + [\text{Fe II}] \lambda 25.9$ ,  $[\text{Si II}] \lambda 34.8$  and 15-25  $\mu\text{m}$  continuum, obtained from the IRS spectral map. All images have been background subtracted. The contour in each image shows the outline of G292.0+1.8 in *Chandra* 0.3-8.0 keV X-rays. The red arrows indicate prominent regions where ejecta are detected both in IR emission lines and in 15-25  $\mu\text{m}$  continuum emission, with the latter revealing regions where dust has formed in the SN ejecta. The blue arrows mark the locations of prominent FMKs.

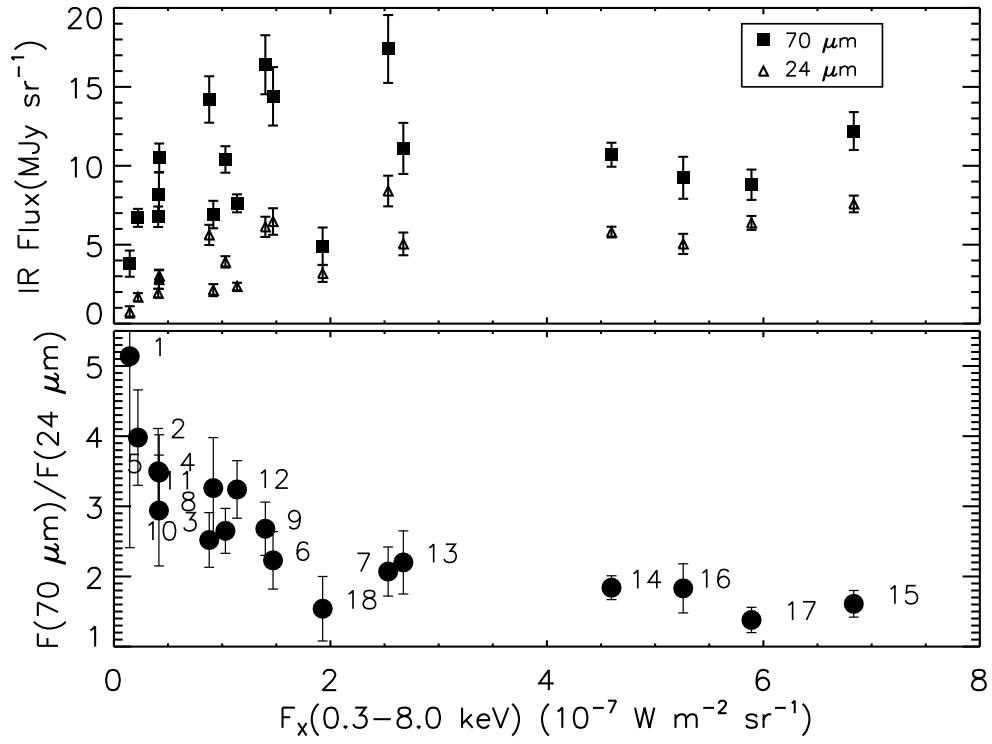


FIG. 5.— Top: the MIPS  $24 \mu\text{m}$  and  $70 \mu\text{m}$  surface brightness shown versus X-ray surface brightness for the flux extraction regions marked in Figure 3. The X-ray surface brightness estimates assume shocked CSM, with a  $kT = 0.75 \text{ keV}$  APEC plasma model,  $N_H = 6 \times 10^{21} \text{ cm}^{-2}$  and abundances 0.2 times solar. The narrow tail (Region 19) exhibits no discernible X-ray emission and is omitted from the plot. Bottom: the  $70/24$  flux ratios for the same regions, shown versus X-ray surface brightness.

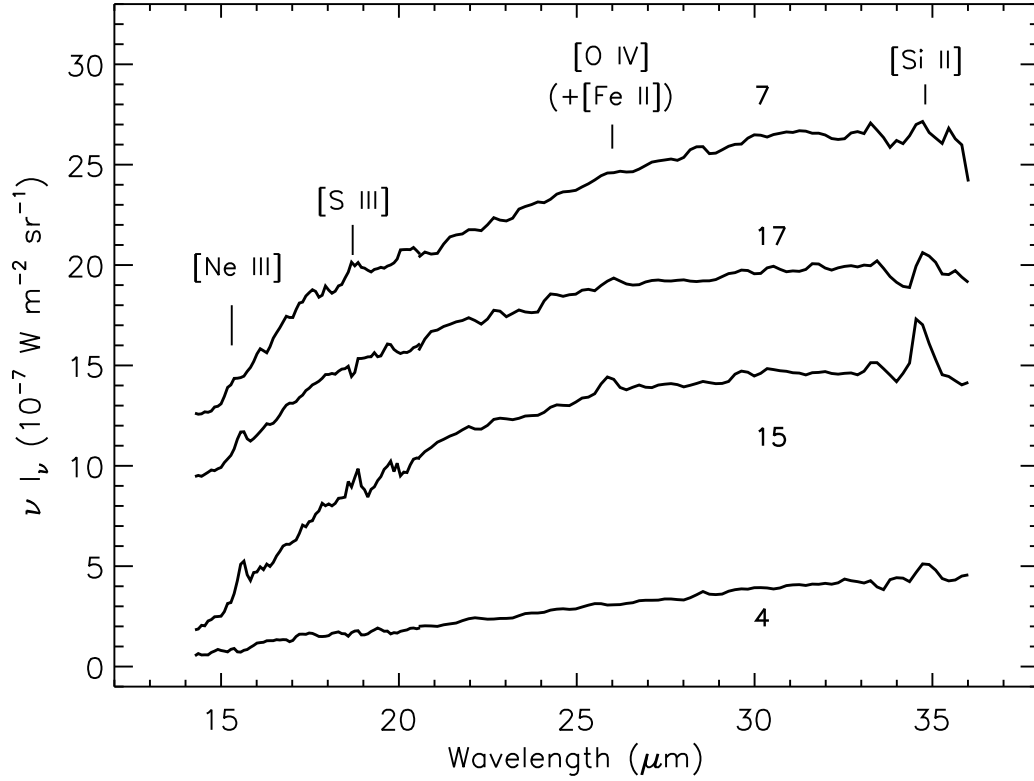


FIG. 6.— A sample of background-subtracted IRS mapping spectra of G292.0+1.8, acquired from selected regions in Figure 3, as labeled. The subtracted background is the average of the emission on the eastern and western sides of the G292.0+1.8 (marked by the two cyan boxes in the left-most panel of Figure 3). The spectra have been shifted in flux to avoid overlap, with Regions (4,7,15,17) being shifted by (0,10,0,7) units in  $\nu I_\nu$ . The emission from each spectrum is dominated by shocked CSM dust continuum, with the coldest dust found along the blast wave filaments (Region 4) and the hottest dust found in the emission clump above the eastern edge of the equatorial belt (Region 17). In addition to the CSM continuum in Region 15, the spectrum at that location also shows faint emission from [Ne III], [S III], [O IV]+[Fe II] and [Si II]. These lines are produced in slower, partially radiative shocks in the equatorial belt (Park et al. 2002, 2004, Ghavamian et al. 2005).

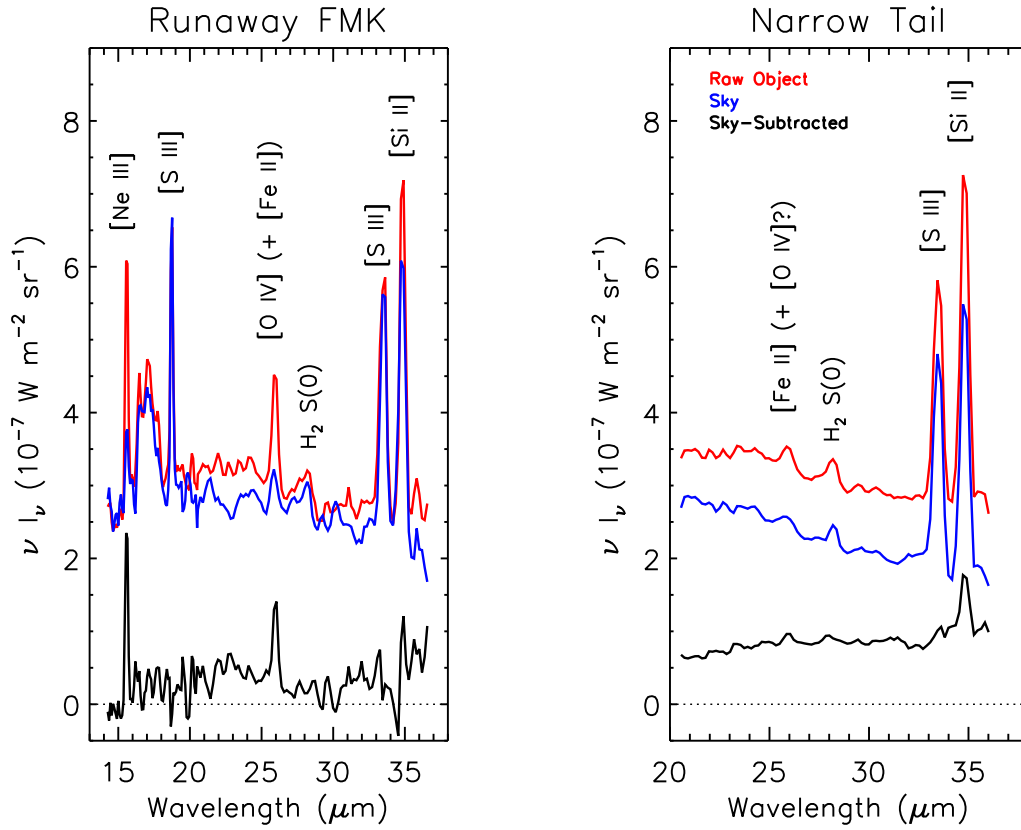


FIG. 7.— Extracted IRS mapping spectra of two features in G292.0+1.8. Left: combined LL2 and LL1 spectra of the southernmost FMK, showing the raw object spectrum (red), the sky spectrum extracted from a nearby section of sky off the SNR (blue), and the resulting sky-subtracted object spectrum (black). The raw object and sky spectra have both been shifted by -2.0 units along the Y axis. Right: The LL1 spectrum of the narrow tail of G292.0+1.8, with similar color schemes for the raw, sky and sky-subtracted object spectrum. The sky spectrum shows emission features from intervening PDR and H II regions along the line of sight to G292.0+1.8: PAH emission at 16.4 and 17.0  $\mu\text{m}$ , as well as H<sub>2</sub> S(1) 17.1  $\mu\text{m}$  and H<sub>2</sub> 28.2  $\mu\text{m}$  emission. The raw object and sky spectra have both been shifted by +2.0 units along the Y axis.